Electric-field-induced ion evaporation from the ionic liquid–vacuum interface ⊕ ⊘
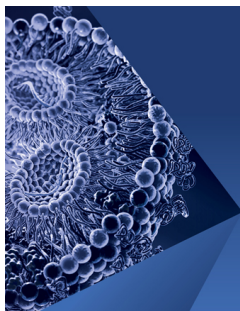
Xianzan Tao; Xikai Jiang ✉ ⓘ

Check for updates

View Online

Export Citation

08 April 2024 03:51:02

Physics of Fluids

Special Topic:

Flow and Lipid Nanoparticles

Guest Editors: Richard Braatz and Mona Kanso

Submit Today!

AIP Publishing

AIP Publishing

Electric-field-induced ion evaporation from the ionic liquid–vacuum interface (EP)

View Online   Export Citation   CrossMark

Xianzan Tao and Xikai Jiang[a] (iD)

AFFILIATIONS

State Key Laboratory of Nonlinear Mechanics, Institute of Mechanics, Chinese Academy of Sciences, Beijing 100190, China and School of Engineering Science, University of Chinese Academy of Sciences, Beijing 100049, China

[a]Author to whom correspondence should be addressed: xikaij@imech.ac.cn

ABSTRACT

We studied ion evaporation from a planar interface between the room-temperature ionic liquid (RTIL) and vacuum under external electric fields by using molecular dynamics (MD) simulations. We calculated the ion evaporation rate (j_e) as a function of the electric field normal to the RTIL surface (E_n), and results under Langevin, dissipative particle dynamics (DPD), and Berendsen thermostats were compared. It was found that DPD thermostat is more suitable for simulating the ion evaporation phenomenon. We also compared results under different methods for applying the electric field (constant potential, constant charge, and constant field methods) and found that j_e-E_n curves from the three methods agree with each other. Temporal evolution of electric fields in vacuum was further analyzed, and variations of electric fields over time were traced to the induced electric field between the evaporated ion and RTIL film. This work could guide the selection of proper methods for MD simulations of electrospray in the pure ion regime and lays the foundation to study more complex electrospray phenomena using MD simulations.

I. INTRODUCTION

The deformation and breakup of fluids in electric fields have been subjected to research for a long time.[1,2] More than four centuries ago, the cone formation on water drops through electrostatic attraction was observed and documented by Gilbert.[3] In 1882, Lord Rayleigh published a seminal work on the critical condition for the breakup of a charged droplet.[4] Now known as the Rayleigh limit, the maximal amount of charge a spherical droplet could carry is $q_R = 8\pi(\epsilon\gamma R^3)^{1/2}$, where ϵ is the permittivity of the surrounding medium, γ is the surface tension of the liquid, and R is the droplet radius. In the 1910s, Zeleny performed pioneering experiments on the behavior of droplets at the end of a capillary in electric fields and made the first documented visual observation of electrospray.[5,6] Later in 1964, Taylor made significant contributions to the understanding of liquid surface instability in electric fields: he showed theoretically that a conical interface between two fluids can exist in equilibrium, which is called the Taylor cone, but only when the cone has a semi-vertical angle 49.3°.[7]

The magnitude of the electric field is important in determining the operating mode of electrospray, such as dripping and cone-jet.[8–13] When the maximal electric field on the liquid surface reaches values of the order of 1 V/nm, ions start to escape from the liquid into the vacuum or gas, which is known as the phenomenon of ion

evaporation.[14,15] When only ions are produced from the Taylor cone, the electrospray is in a pure ion regime.[16] Early attention on ion evaporation from liquids is due to its applications in areas such as atmospheric environment and electrospray of liquid metals.[17,18] As a normal atmospheric process, electrified droplets in clouds release ions into the atmosphere through ion evaporation, with important consequences for climate and precipitation.[19] Electrospray of liquid metals operating in the pure regime is a liquid metal ion source, which can produce focused ion beams with applications in the semiconductor industry.[20] Ion evaporation was first observed by Chapman in the 1930s, when he studied the carrier mobility spectra of liquids electrified by bubbling and spraying extensively using experiments.[21–23] In the 1970s, Iribarne and Thomson made new measurements on the mobility spectra with a different arrangement and higher resolution and also investigated evaporated ions using a mass spectrometer system.[14,17] In addition to experiments, they developed a theory to explain the mechanism of ion evaporation. In the theoretical model, ion evaporation is treated as a kinetic process, and ions must overcome an energy barrier above the liquid surface in order to evaporate from a charged droplet. They estimated the Gibbs' free energy of solvation of cluster ions; based on this estimate, the energy barrier was discussed, by treating the kinetic process as a first-order reaction and using the absolute

reaction rate theory.[14] Later in the 1990s, Loscertales and de la Mora performed experiments on kinetics of field evaporation of ions from droplets, confirming that small ions in electrospray ionization are produced by field-emission; they also found that ionization rates agree well with the results from the polarization potential model of Iribarne and Thomson, in which attraction between the evaporating ion and liquid surface is due to polarization of the dielectric liquid by the ion.[15]

Ion evaporation from liquid metals was widely studied since its discovery in the 1960s.[24] Research and development on liquid metal ion source have led to successful industrial applications such as focused ion beam technologies.[25] However, less attention was paid to electrospray of volatile nonmetallic liquids in the pure ion regime, due to the difficulty to achieve and control such operation.[26,27] In 2003, the paradigm begins to shift when electrospray of room-temperature ionic liquids (RTILs) was found to attain the pure ion regime and be used as ionic liquid ion sources.[26] RTILs are a class of electrolytes that are made entirely of ions but remain in a liquid state at room temperature.[28] They exhibit unique physicochemical properties such as low vapor pressure, high thermal stability, and wide electrochemical window.[29,30] Numerous types of RTILs can be synthesized, offering vast combinations of cations and anions. Due to these remarkable properties, an ionic liquid ion source can produce ion beams with diverse and tailorable ion species, excellent brightness, and wide range of mass/charge ratios, making it potential solution to long-standing challenges in fields such as space propulsion and focused ion beam applications.[31–33]

In the last two decades, experiments have been performed to study ion evaporation from RTILs. Lozano and Martinez-Sanchez successfully achieved ion emission from ionic liquid ion sources without electrochemical reactions, by alternating the voltage of power supply such that the potential difference across the electrical double layer (EDL) at liquid–metal interface is below the electrochemical window.[34] Ku and de la Mora used high resolution differential mobility analysis to study clusters formed in positive electrosprays of several RTILs A^+B^- dissolved in acetonitrile; the ionization mechanism for the formation of small clusters $(A^+)(AB)_n$, with n values typically from 0 to 3 and peaking at about $n = 1$, is attributed to ion evaporation.[35] Chiu et al. performed mass spectrometric analysis of colloid thruster ion emission from 1-ethyl-3-methylimidazolium tetrafluoroborate ([EMIM][BF$_4$]), and identified X([EMIM][BF$_4$])$_n$ ($n = 0$, 1, 2) ions, where X $=$ EMIM$^+$ or BF$_4^-$.[36] In another study, Chiu et al. analyzed positive and negative vacuum electrospray currents from EMIM-bis (trifluoro-methylsulfonyl)imide ([EMIM][Im]) wetted on a sharp tungsten needle and observed pure ion emission at emission angles larger than ~15°; their results demonstrated that ions are produced in an Iribarne–Thomson field-evaporation mechanism at the transition region between the Taylor cone and jet.[37] In the study by Guerrero et al., by using time-of-flight mass spectrometry, ion emissions from different propylene carbonate solutions mixed with either of [EMIM][BF$_4$] or [EMIM][Im] were analyzed; measured ion currents were compared to predictions from ion evaporation theory, and an anomalously low activation energy was found, which could be due to the pure cone-jet electric field in the scaling laws used for the pure cone-jet regime.[38] Hogan and de la Mora conducted tandem ion mobility-mass spectrometry study of ion evaporation from ionic liquid-acetonitrile nanodrops, showing that the charge loss mechanism is ion evaporation.[39] To eliminate droplet emission, Perez-Martinez and Lozano introduced

porous carbon based on resorcinol-formaldehyde xerogels as an emitter substrate and demonstrated that it can be shaped to required micrometer-sized geometries and has appropriate transport properties to favor pure ion emission from RTILs.[40]

Apart from experiments, theoretical and numerical methods were also used to provide details and insight on the phenomenon of ion evaporation from RTIL surfaces. Based on order-of-magnitude analysis, Higuera developed a qualitative model of ion evaporation in the meniscus of an ionic liquid ion source operating in the pure ion regime: the model predicted that the ion evaporation current is limited by the finite conductivity of the RTIL rather than by the space charge around its surface; the current/applied field characteristic shows a region of very weak ion evaporation when the applied field is below a certain starting value, and a conduction-controlled region for higher values of the applied field.[41] Coffman et al. treated the RTIL as a leaky dielectric liquid and numerically solved electrohydrodynamic equations; they found that the feeding flow may be important in ion evaporation characteristics, and in contrast to the widespread notion, the cone's semi-vertical angle in the pure ion regime is not the ubiquitous 49.3°.[42] In a subsequent work, Coffman et al. developed a detailed electrohydrodynamic model to simulate the behavior of a stationary RTIL meniscus undergoing ion evaporation; they found that the meniscus is Stokesian and hydrostatic and governed by conduction, and the applied electric field affects both the emission current and the shape of the meniscus.[43] Later on, Gallud and Lozano included field-enhanced thermionic emission in the electrohydrodynamic model to simulate RTIL menisci during ion evaporation; static stability of numerical solutions was studied when the external field, hydraulic impedance, meniscus dimension, and liquid temperature are varied.[44] Recently, Misra and Gamero-Castaño developed a continuum phase field electrohydrodynamic model to study the interplay between Coulomb explosions and ion emission for charged RTIL nanodroplets; they found that when the droplet diameter is less (larger) than 45 nm, ion emission can (cannot) suppress Coulomb explosion.[45]

Being able to describe the discrete nature of the ion and capture ion evaporation with sufficiently high spatiotemporal resolution, molecular dynamics (MD) simulations have been utilized to study nanoscale breakup and deformation of RTILs in electric fields. Daily studied dynamics of small droplets of [EMIM][BF$_4$] in large external electric fields using MD simulations, and results indicated that the Taylor expression using macroscopic surface tensions for the critical electric field strength is order-of-magnitude-correct.[46] Prince et al. performed MD simulations of small clusters and nanodroplets of [EMIM][Tf$_2$N] in external electric fields and found that critical electric field for ion emission is 0.985 V/nm, which agrees with the experimental value of 1.0 V/nm; they also found excellent agreement between simulations and experiments in the composition of ion emission for a neutral 125-ion-pair droplet at an electric field strength of 1.2 V/nm.[47] Borner et al. carried out a series of MD simulations on the capillary electrospray of RTILs, finding that one of the coarse-grained model can predict the formation of the Taylor cone, the cone-jet, and other extrusion modes; the influence of electrical boundary conditions on the operating mode and ion emission sites was also investigated.[48–50] Mehta and Levin compared MD electrospray simulations of two RTILs, ethylammonium nitrate (EAN) and ethanolammonium nitrate (EOAN), and found that combination of higher energy storage and stronger hydrogen bonds in the N-C$_1$-C$_M$ covalent angle in EAN

results in a stronger resistance of ion emission from the bulk compared to EOAN.[51] They also compared simulations of [EMIM][BF$_4$] and EAN, and the results suggested that [EMIM][BF$_4$]-based colloid thrusters tend to operate in ion mode while EAN-based devices tend to operate in the droplet mode.[52] In a following work, they compared the influence of different electrostatic solvers on MD electrospray simulations, showing that the direct Coulomb method with a sufficiently large cutoff radius is most accurate, but it is computationally expensive; it was also observed that domain periodicity greatly affects the accuracy of capillary electrospray simulations.[53] More recently, they developed an octree-based electrostatic solver to model the electrospray of RTILs in MD simulations and observed that the octree-based method produces different results on ion emission compared to that obtained by the direct Coulomb method.[54]

Electrospray of RTILs was also studied by using multiscale models. Nuwal *et al.* combined MD and particle-in-cell (PIC) simulations to study fragmentation in an electrospray plume: a dimer fragmentation model was developed from MD simulations of [EMIM][BF$_4$], and the model was then implemented in the PIC simulations.[55] Asher *et al.* combined an MD model, a particle-particle model, and a PIC model to study electrospray of [EMIM][BF$_4$] from porous emitter tips; their results showed that the activation of multiple emission sites causes a noticeable increase in the beam's spread, leading to increased intercepted current.[56] Petro *et al.* simulated a single-emitter electrospray plume of [EMIM][BF$_4$] in a positive pure ion mode by combining electrohydrodynamic fluids and *n*-body particle modeling, in which MD simulations and experimental data were used to develop an ion fragmentation model for capturing metastable nature of ion clusters.[57]

In this study, we focus on MD simulations of ion evaporation from the RTIL surface. In a prior work,[58] we have analyzed electric-field-driven ion evaporation from the free surface of a planar RTIL film: the relationship between ion evaporation current density (j_e) and electric field normal to the RTIL surface (E_n) calculated from MD simulations was found to agree with the ion evaporation theory of Iribarne and Thomson; the formation of monomers and dimers was traced to the metastable states of evaporating ions near the RTIL–vacuum interface. Despite aforementioned progress, there are still issues to be addressed in MD simulations of ion evaporation from the RTIL–vacuum interface in electric fields. For MD simulations in an NVT ensemble, thermostats that control the liquid temperature may have significant influence on the transport phenomena.[59] How different thermostat strategies and temperatures affect the phenomenon of ion evaporation remains to be answered. To drive ion evaporation, an electrical potential difference along the direction of ion evaporation and the resulting E_n need to be applied in the simulation system. There are different methods to generate the potential difference and the electric field normal to the liquid surface, and how these methods affect the ion evaporation process needs to be explored. Furthermore, in the process of ion evaporation, the time interval between two adjacent ion evaporation events may vary. How ion evaporation evolves as a function of time and how evaporating ions in turn affect the electric field need further investigations.

The remainder of this work is organized as follows: Sec. II discusses details of the MD simulation system, thermostat algorithms, and methods for applying the electric field. In Sec. III, we present and compare relationships between ion evaporation current density (j_e) and E_n obtained by using different thermostats, temperatures, and

strategies for applying the electric field. Temporal evolution of E_n will also be analyzed to provide more details of the ion evaporation phenomenon. In the end, we conclude with key take-home messages.

II. METHOD

We perform MD simulations to study electric-field-induced ion evaporation from the RTIL–vacuum interface by using the ESPResSo package.[60] Figure 1 shows the MD simulation system, which contains two planar electrodes (yellow) and a planar RTIL film (blue) with a thickness of ~7 nm placed on the bottom electrode. The thickness of the RTIL film is large enough to ensure that EDLs near the bottom electrode does not affect ion evaporation.[58] The coordinate system and the origin are shown in Fig. 1, and the simulation box (dashed lines) measures $7 \times 7 \times 50$ nm^3 ($x \times y \times z$). There is a 5 nm gap between the top electrode and the top of the simulation box in the z-direction due to the requirement of the electrostatic layer correction method, which is used for computing electrostatic interaction in the simulation system.[61–63] Different from the three-dimensional Ewald method with a correction term for the slab geometry that requires the gap size to be at least with a length of L_x or L_y (L_x and L_y are lateral dimensions of the simulation box),[64] there is no special requirement on the gap size in the electrostatic layer correction method except that it is larger than zero.[61] In this work, the gap size is 0.1 times the height of the simulation box, which gives reasonable accuracy according to Fig. 4(b) in Ref. 61. Periodic boundary conditions (PBC) are applied in x- and y-directions. In this work, 1-butyl-3-methylimidazolium hexafluorophosphate ([BMIM][PF$_6$]), one of the most commonly used RTILs, is considered. A four-site coarse-grained model is used to simulate [BMIM][PF$_6$]. This model is computationally efficient compared to all-atom models, while it can still capture key dynamic properties of the RTIL.[58] Detailed force-field parameters of the coarse-grained model can be found in Ref. 65. In our MD simulations, the time step is 0.002 ps, and the equation of motion is integrated using the velocity Verlet algorithm.[60]

To drive ion evaporation, an external electric field normal to the liquid surface should be applied in the simulation system. Here, three strategies for generating the field are considered: constant potential, constant charge, and constant field methods. In the constant potential
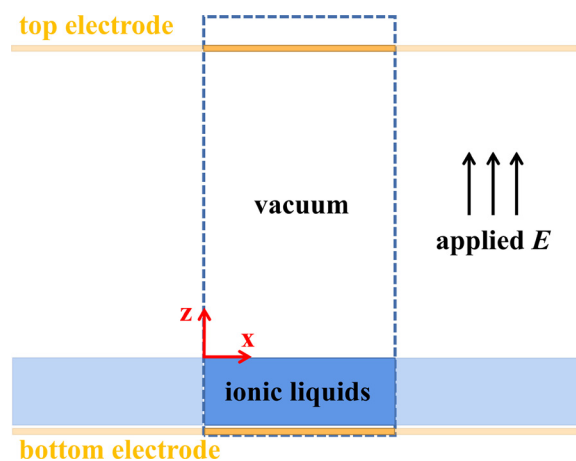

FIG. 1. Schematic of the simulation system. *E* denotes the external electric field.

method, the electrical potential (ϕ) on each electrode is maintained at a constant value.[66] The electrostatic layer correction with image charges method, which accounts for 2D electrostatics and charge induction by evaluating the image charges every time step, is used to realize that the electrodes are in the constant potential state.[67] In our cases, ϕ on the bottom electrode is 0 V, and ϕ on the top electrode is V_0. As the electrodes and RTIL film are planar and the simulation box is periodic in x- and y-directions, we consider the system as quasi-one-dimensional and focus on the electrical potential along the z-direction. Using boundary conditions for ϕ at two electrodes to solve Poisson's equation,[68] we obtain the electrical potential at any z-position between electrodes as

$$\phi(z) = -\frac{1}{\epsilon_0}\left[\int_0^z (z-u)\rho_e(u)\mathrm{d}u - z\int_0^L\left(1-\frac{u}{L}\right)\rho_e(u)\mathrm{d}u\right] + \frac{z}{L}V_0, \tag{1}$$

where $L = 45$ nm is the distance between electrodes along the z-direction, ϵ_0 is the vacuum permittivity, and ρ_e is the ionic space charge density. In the constant charge method, charges are uniformly distributed on every wall atom to generate desired surface charge densities (s) on the electrodes. In the positive mode, the lower (upper) electrode is positively (negatively) charged; in the negative mode, the lower (upper) electrode is negatively (positively) charged. Using surface charge densities as boundary conditions to solve the Poisson equation,[68] the electrical potential at any z-position can be calculated as

$$\phi(z) = -\frac{1}{\epsilon_0}\left[\int_0^z (z-u)\rho_e(u)\mathrm{d}u - sz\right]. \tag{2}$$

In the constant field method, a constant external electric field (E_{ext}) is applied to every charged atom in the simulation system. By using Eq. (2) with zero wall charge density and superpositioning the potential caused by E_{ext}, we obtain $\phi(z)$ as

$$\phi(z) = -\frac{1}{\epsilon_0}\int_0^z (z-u)\rho_e(u)\mathrm{d}u + E_{\mathrm{ext}}z. \tag{3}$$

The distribution of electric field along the z-direction can then be determined by differentiating the electrical potential with respect to z. In the negative/positive mode, the electrical potential difference between two electrodes ranges from ± 40 to ± 110 V for constant potential simulations; the external electric field ranges from $+1.11/-1.56$ to ± 2.89 V/nm for constant field simulations; the wall surface charge density ranges from ± 0.014 to ± 0.026 C/m^2 for constant charge simulations.

In this study, we compare the results from MD simulations using three different thermostat strategies: Langevin thermostat, dissipative particle dynamics (DPD) thermostat, and Berendsen thermostat. The Langevin thermostat starts from the classical Langevin equation

$$\mathrm{d}\boldsymbol{p}_i = \boldsymbol{f}_i\mathrm{d}t - \gamma\boldsymbol{p}_i\mathrm{d}t + \sqrt{2\gamma m k_B T}\mathrm{d}\boldsymbol{w}_i, \tag{4}$$

where $\boldsymbol{p}_i$ is the momentum of the ith particle, $\boldsymbol{f}_i = \sum_{j(\neq i)}\boldsymbol{f}_{ij} + \boldsymbol{f}_{ext}$ contains deterministic forces exerted on the ith particle due to particle–particle interactions and external fields, and t is the time.[69] The second term on the right-hand-side of Eq. (4) is contributed by the frictional force and γ is the damping constant; the last term is the contribution from random forces, and $\sqrt{2\gamma m k_B T}$ is related to the

damping constant through the fluctuation-dissipation theorem, where m is the particle's mass, k_B is the Boltzmann constant, and T is the temperature.[59] In the last term, $\boldsymbol{w}_i = \sqrt{\mathrm{d}t}\boldsymbol{G}_i$, and each component of $\boldsymbol{G}_i$, $G_{i\alpha}$ is an independent Gaussian random variable satisfying

$$\langle G_{i\alpha}\rangle = 0, \quad \langle G_{i\alpha}G_{j\beta}\rangle = \delta_{ij}\delta_{\alpha\beta}, \tag{5}$$

where $\langle\ldots\rangle$ is the ensemble average, i and j denote the ith and jth particles, α and β are spatial coordinates, and δ_{ij} is the Kronecker delta function.[69] From a physical perspective, the frictional forces cool the system while the random forces (thermal forces) heat the system.

DPD was originally developed as a method for simulating hydrodynamic interactions in fluids at mesoscale.[70] It was later extended to be used as a thermostat method in MD simulations, where frictional and random forces acting on each particle are related to its neighboring particles.[71] The equation of motion for particles under the DPD thermostat is

$$\mathrm{d}\boldsymbol{p}_i = \boldsymbol{f}_i\mathrm{d}t + \xi\mathrm{d}t\sum_{j(\neq i)}\boldsymbol{V}_{ij} + \sqrt{2\gamma m k_B T}\sum_{j(\neq i)}\mathrm{d}\boldsymbol{W}_{ij}, \tag{6}$$

where $\xi = m\gamma$ is the friction coefficient, $\boldsymbol{V}_{ij}$ is related to the relative velocity between ith and jth particles, and $\mathrm{d}\boldsymbol{W}_{ij}$ contributes to the random forces. $\boldsymbol{V}_{ij}$ and $\mathrm{d}\boldsymbol{W}_{ij}$ can be expressed as

$$\boldsymbol{V}_{ij} = \varphi^D(\boldsymbol{r}_{ij})(\boldsymbol{v}_{ij}\cdot\hat{\boldsymbol{r}}_{ij})\hat{\boldsymbol{r}}_{ij}, \quad \mathrm{d}\boldsymbol{W}_{ij} = \varphi^R(\boldsymbol{r}_{ij})\mathrm{d}w_{ij}\hat{\boldsymbol{r}}_{ij}, \tag{7}$$

where $\boldsymbol{r}_{ij} = \boldsymbol{r}_i - \boldsymbol{r}_j$ is the position vector between the ith and jth particles, $\hat{\boldsymbol{r}}_{ij} = \boldsymbol{r}_{ij}/|\boldsymbol{r}_{ij}|$ is the unit vector, and $\boldsymbol{v}_{ij} = \boldsymbol{v}_i - \boldsymbol{v}_j$ is the relative velocity. $\mathrm{d}w_{ij} = \mathrm{d}w_{ji}$ are independent Wiener processes, and $\varphi^D(\boldsymbol{r}_{ij})$ and $\varphi^R(\boldsymbol{r}_{ij})$ are weight functions[71]

$$\varphi^D(\boldsymbol{r}_{ij}) = \varphi^R(\boldsymbol{r}_{ij}) = \begin{cases} 1, & r_{ij} < r_c \\ 0, & r_{ij} \geq r_c \end{cases}, \tag{8}$$

where $r_{ij} = |\boldsymbol{r}_{ij}|$ and $r_c = \sigma_i + \sigma_j$ is the cutoff radius. σ_i and σ_j are van der Waals radii for ith and jth atoms in Lennard-Jones parameters of the coarse-grained force field for [BMIM][PF$_6$].[65] Compared with the Langevin thermostat, DPD thermostat conserves local and linear momentum of the system and satisfies Galilean invariant, which makes it more suitable for studying transport phenomena in MD simulations.[59,72]

In Berendsen thermostat, the temperature is controlled by scaling the momenta of all particles as

$$\boldsymbol{p}' = \boldsymbol{p}\sqrt{1 + \frac{\Delta t}{\tau}\left(\frac{T}{T_c} - 1\right)}, \tag{9}$$

where $\boldsymbol{p}'$ and $\boldsymbol{p}$ are the momenta after and before scaling, respectively, Δt is the time step, τ is the coupling parameter or time constant that determines how tightly the system and the heat bath are coupled, T is the prescribed liquid temperature, and T_c is the current kinetic temperature.[69]

In our MD simulations, the electric current density along the z-direction (j_e) is calculated by dividing the total amount of charges crossing a detection plane 5 nm below the top electrode by the cross section area (7×7 nm^2) of the simulation box and the total simulation time. When the evaporated ion is within 5 nm away from the top electrode, it is removed from the simulation system; at the same time, one counterion near the bottom electrode is also removed, in order to

satisfy the electrostatic neutrality of the simulation system. For each case with a specific combination of E_n, thermostat strategy, and the method for applying E_{ext}, seven independent simulations are performed to improve statistical sampling.

III. RESULTS AND DISCUSSION

Figure 2 shows snapshots from MD simulations for ion evaporation processes from the RTIL–vacuum interface. In Fig. 2(a), cation is evaporated, and V_0 is -80 V; in Fig. 2(b), anion is evaporated, and V_0 is 80 V. In each case, five snapshots are shown, and the time interval between adjacent snapshots is 1.2 ps. At $t = 0$ ps ($t = 0$ and 1.2 ps), the cation (anion) being evaporated has moved to the top of the RTIL–vacuum interface. At $t = 1.2$ (2.4) ps, the cation (anion) is about to escape from the interface and exhibits a fingerlike structure. From

$t = 2.4$ (3.6) to 4.8 ps, the cation (anion) is in vacuum and becomes further away from the interface under the action of the external electric field.

Figure 3 shows variations of $|j_e|$ as a function of $|E_n|$ from constant potential simulations using Langevin, DPD, and Berendsen thermostats, respectively. For Langevin thermostat, γ is set to 1; for DPD thermostat, ξ is chosen as 50. The results under Berendsen thermostat are from Ref. 58. The temperature of the RTIL film is 400 K. It can be seen that, under different operating modes and thermostats, the general trend remains the same that $|j_e|$ increases as $|E_n|$ increases. This is because, as $|E_n|$ increases, the external force along the z-direction exerting on the evaporating ion becomes larger, and it becomes easier for the evaporating ions to overcome the energy barrier near the RTIL surface. It is also observed that, at the same $|E_n|$, $|j_e|$ in the negative
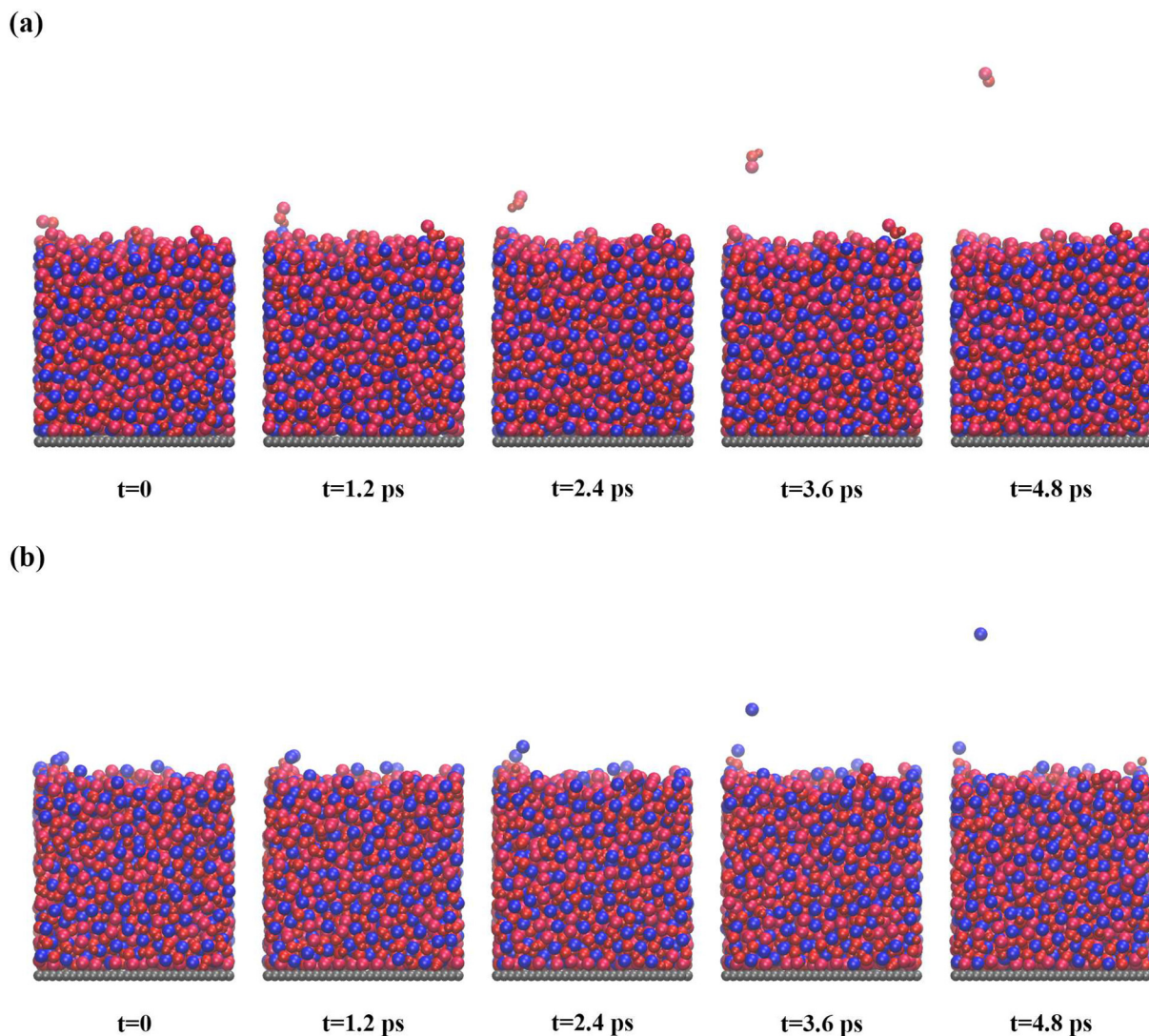
(a)

| t=0 | t=1.2 ps | t=2.4 ps | t=3.6 ps | t=4.8 ps |

(b)

| t=0 | t=1.2 ps | t=2.4 ps | t=3.6 ps | t=4.8 ps |

FIG. 2. Snapshots from MD simulations showing ions evaporating from the RTIL–vacuum interface. Red (blue) color denotes cation (anion) atom. Liquid temperature is 400 K. The external electric field is generated by the constant potential method, and V_0 are (a) -80 and (b) 80 V, respectively.
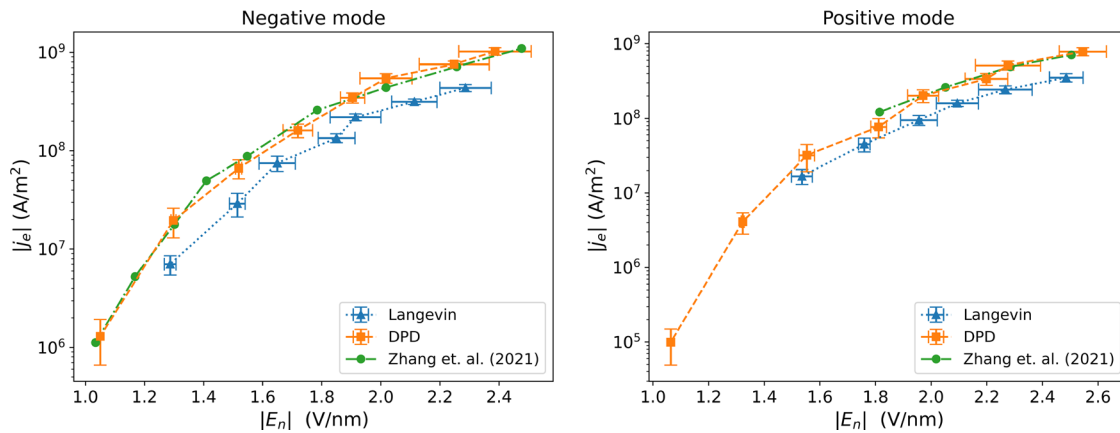
FIG. 3. $|j_e|$ as a function of $|E_n|$ under Langevin (blue) and DPD (orange) thermostats. The results in Ref. 58 under Berendsen thermostat (green) are also shown.

mode (anion evaporation) is larger than that in the positive mode (cation evaporation). This is mainly caused by two reasons. First, compared to the anion, the cation's molecular structure is more complex, and its volume is larger, and the Gibbs free energy of solvation of the cation is larger, which makes it more difficult for cations to evaporate from the RTIL surface. Second, the mass to charge ratio for the cation is larger than that for the anion, and under the same external electric field, the cation is more difficult to accelerate in vacuum compared to the anion. When $|E_n| < 1.5$ V/nm, the increasing rate of $|j_e|$ with $|E_n|$ is larger than that when $|E_n| > 1.5$ V/nm. This is mainly caused by structural changes of the RTIL/vacuum interface at higher $|E_n|$: the ion density distribution across the surface becomes wider and the magnitude of ion density decreases; these structural changes lead to the decrement in the dielectric constant of the RTIL/vacuum interface.[58,73] Figure 3 also includes statistical errors of j_e and E_n, and the error in E_n (j_e) is found to increase (decrease) as $|E_n|$ increases in general. At relatively high $|E_n|$, more ions are evaporated into the vacuum per unit time, resulting in increased sampling size and hence improved statistics of j_e; on the other hand, more evaporating ions near the RTIL surface induce more disturbance on E_n, which leads to larger error in E_n.

Comparing the results under different thermostats, we can see that at a certain $|E_n|$, $|j_e|$ under Langevin thermostat is the smallest in either operating mode. This is mainly because Langevin thermostat is applied to every ion in the system and ions in vacuum are also affected by frictional forces. The frictional force acts in the opposite direction of the driving force due to the external electric field and becomes larger as ion velocity increases. Several different γ (0.5, 1, 5, 10) in Langevin thermostat when $V_0 = 100$ V are tested to study its effect on ion evaporation rate, and the average $|j_e|$ are found to be 4.80×10^8, 3.16×10^8, 0.869×10^8, and 0.445×10^8 A/m², respectively. As γ increases from 0.5 to 10, $|j_e|$ decreases notably due to the increased frictional force. In DPD thermostat, however, frictional and random forces based on pair-wise interactions vanishes as the evaporating ion moves away from the RTIL–vacuum interface. From Fig. 3, it can also be seen that the results under DPD and Berendsen thermostats agree reasonably well with each other in both positive and negative modes. However, the two thermostat strategies are fundamentally different, and caution needs to be exercised while using the Berendsen

thermostat for MD simulations of electrospray. The Berendsen thermostat rescales momenta of all ions in the system: when the number of evaporating ions per unit time is relatively small, their contributions to the total kinetic energy of the simulation system are marginal, resulting in minor effect of rescaling momenta on ion dynamics in vacuum and j_e. When the number of evaporating ions per unit time becomes large enough, their contributions to the total kinetic energy become innegligible, and it will lead to considerable influence of rescaling momenta on ion dynamics in vacuum and j_e; as the average kinetic energy of an evaporating ion in vacuum is generally larger than that of an ion in the bulk liquid, rescaling momenta in Berendsen thermostat will reduce ion velocities in vacuum and hence j_e. In this work, as the number of evaporating ions is relatively small, rescaling momenta of all ions in Berendsen thermostat has minor effect on results. When comparing thermostats, it would be desirable to compare directly to benchmark results. To our knowledge, the only available results in the current literature for the same system are from Ref. 58, in which Berendsen thermostat was used. The agreement between results under Berendsen and DPD thermostats in Fig. 3 leads to more confidence in using these thermostats. Physically speaking, ions' motion in vacuum should not be altered by frictional or random forces from the thermostat. If the amount of atoms in evaporating species (ions or droplets) is comparable to that in the bulk liquid, differences between results under Berendsen and DPD thermostats will be more pronounced. Therefore, we arrive at the conclusion that DPD thermostat is more suitable for simulating ion evaporation from the liquid–vacuum interface compared to Langevin and Berendsen thermostats. In the remainder of this work, we focus on results under DPD thermostat.

The effect of DPD thermostat's friction coefficient ξ on j_e and E_n is also studied. We find that if $\xi < 10$, DPD thermostat cannot maintain the liquid temperature at the desired value. So several different values for $\xi > 10$ are tested, and they are 20, 50, and 80, respectively. In test simulations, the electrical potential differences between the top and bottom electrodes are ± 60, ± 80, and ± 100 V, respectively. The results are presented in Fig. 4. It is observed that, when ξ changes at each applied voltage, j_e and E_n are nearly the same within statistical error. In both positive and negative modes, differences between average values of j_e or E_n under different ξ generally increase as V_0
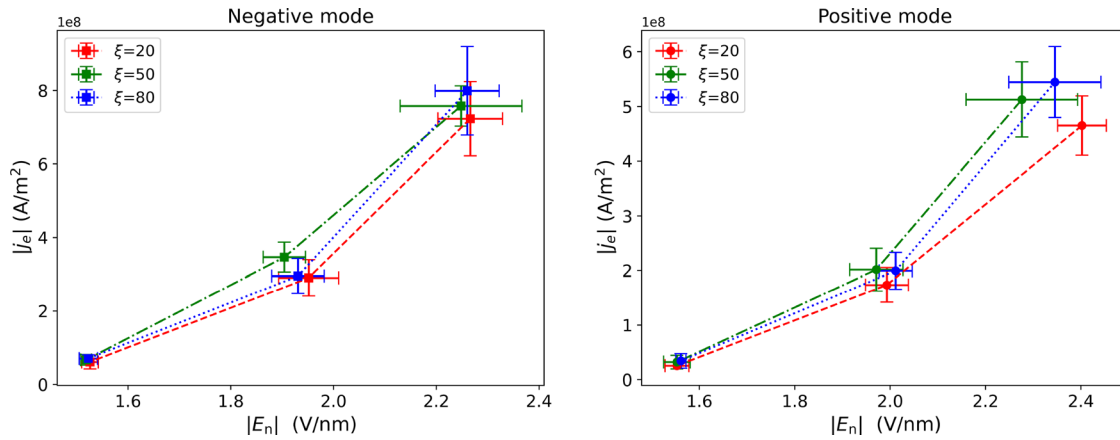
FIG. 4. The effect of DPD thermostat's friction coefficient ξ on j_e and E_n. The electrical potential differences between the top and bottom electrodes are ± 60, ± 80, and ± 100 V, respectively.

increases. Despite these differences in average values at relatively large V_0, varying ξ has minor influence on j_e and E_n in the range of ξ considered here.

By using the DPD thermostat, we study how the liquid temperature affects ion evaporation rates from the RTIL–vacuum interface. Figure 5 shows absolute magnitude of ion current density as a function of the liquid temperature under different applied voltages. The liquid temperature ranges from 300 to 450 K with an interval of 50 K; V_0 we considered are -100, -80, 80, and 100 V, respectively. In this voltage range, E_n are between 1.9 and 2.3 V/nm. This electric field range favors ion evaporation with significantly suppressed droplet emission from Taylor cones of ionic liquids, facilitating the attainment of the pure ion regime.[26] For the temperature range, the force field model developed for [BMIM][PF$_6$] has good agreement with experimental data on density, diffusion coefficient, and viscosity in the range of 300–450 K.[65] Moreover, the electrical conductivity of the ionic liquid in this temperature range varies between 0.53 and 5.6 S/m,[65] which also facilitates the attainment of the pure ion regime.[26] So the voltage and
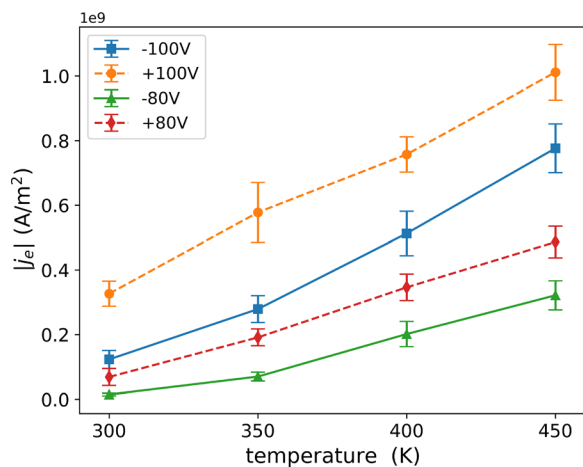
temperature ranges here are selected based on experimental conditions to better achieve the pure ion regime. It can be seen from Fig. 5 that, under a certain applied voltage, j_e increases almost linearly as the liquid temperature increases. This could be caused by three reasons. First, the RTIL's ionic conductivity increases when the liquid temperature increases, resulting in faster ion transport from the bulk to the liquid surface to sustain high ion evaporation rate. Second, the RTIL's viscosity decreases and frictional forces exerted on evaporating ions from the RTIL becomes smaller, making it easier for the ions to move out from the liquid. Third, the thermal energy increases and the surface tension decreases, leading to enhanced roughness $\sqrt{k_B T/\gamma}$ and thermal fluctuation of the RTIL–vacuum interface that can promote ions on the interface to overcome the energy barrier and escape from the liquid surface.[74] At the same temperature, j_e corresponding to different voltages are different. This observation is consistent with results in Fig. 3, and relevant explanations are provided in the discussion of Fig. 3.

We next compare the results from constant potential, constant field, and constant charge simulations. Figures 6(a) and 6(b) show the j_e-E_n relationship from simulations using different methods for generating the external electric field. It is found that, in both positive and negative modes, j_e-E_n curves from these different simulations generally agree well with each other considering statistical errors. This result indicates that, for the type of simulation system considered in this study (a planar liquid film between two planar electrodes), easy-to-implement methods such as constant field and constant charge methods could also be used to investigate electric-field-induced ion evaporation from the liquid–vacuum interface. In common open-source MD software such as LAMMPS[75] and Gromacs,[76] performing constant potential simulations usually requires users to develop their own codes or rely on extra packages, in order to correctly solve the Poisson equation with electrical potential boundary conditions at electrodes.[58,77,78] However, constant field and constant charge simulations are relatively straightforward to realize based on existing features in widely used open-source MD software, without the need to modify the source code or implement new feature into the software by the users.

According to the theory of Iribarne and Thomson, the current density of ion evaporation from the liquid surface satisfies[14,15,43,44]

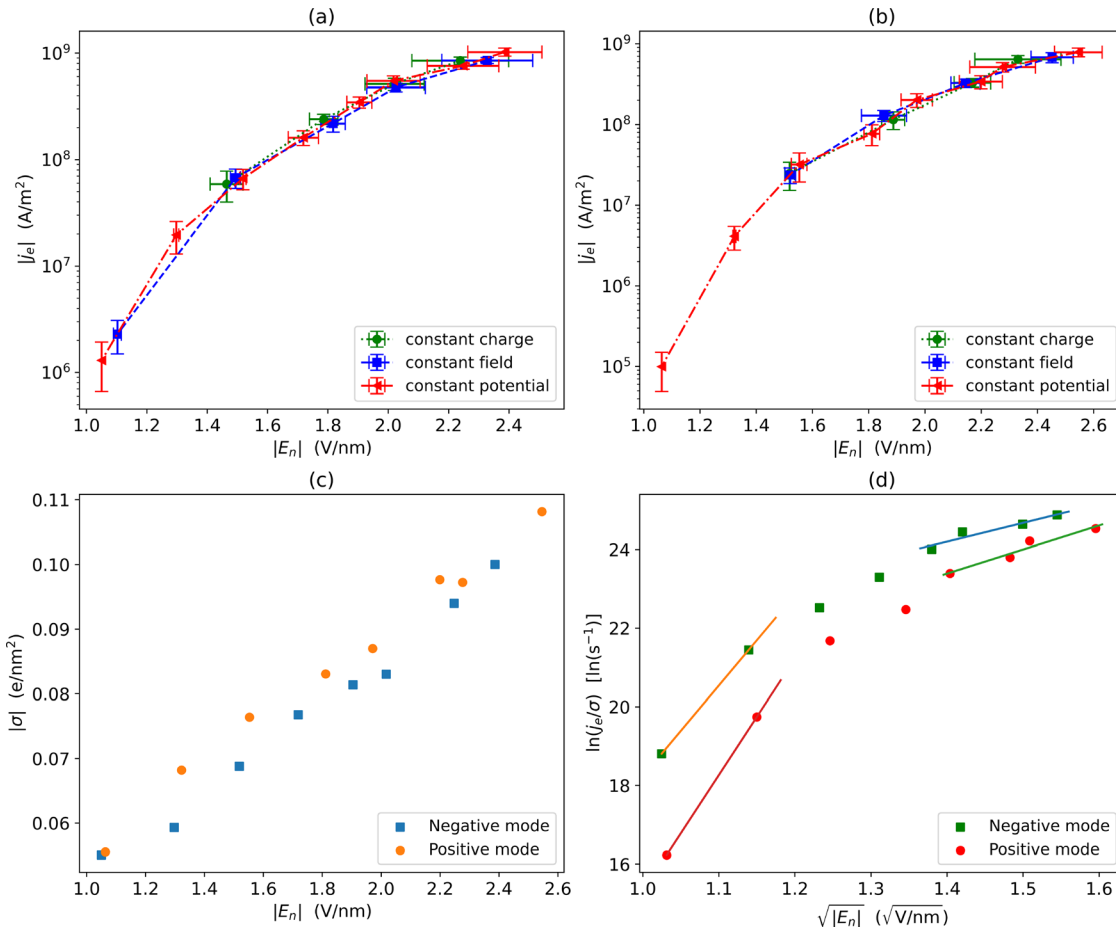**FIG. 5.** $|j_e|$ as a function of the liquid temperature under different applied voltages.

FIG. 6. $|j_e|$ as a function of $|E_n|$ from constant potential, constant charge, and constant field simulations in (a) negative and (b) positive modes. (c) Absolute magnitudes of surface charge densities on the RTIL–vacuum interface ($|\sigma|$) as a function of $|E_n|$. (d) $\ln(j_e/\sigma)$ plotted as a function of $\sqrt{|E_n|}$.

$$j_e = \frac{\sigma k_B T}{h} \exp\left(-\frac{\Delta G - G(E_n)}{k_B T}\right), \quad (10)$$

where h is Planck constant, σ is the surface charge density at the liquid–vacuum interface, ΔG is the evaporation energy barrier for solvated ions, and $G(E_n)$ is the reduction to ΔG as a function of E_n. $G(E_n)$ assumes the form $G(E_n) = \sqrt{\frac{q^3 E_n}{4\pi\epsilon_0} \frac{\epsilon_r - 1}{\epsilon_r + 1}}$, where q is the charge of the evaporating ion and ϵ_r is the dielectric constant of the liquid.[14] In MD simulations, the surface charge density on the RTIL–vacuum interface is calculated by $\sigma = \epsilon_0(E_n^v - E_n^l)$, where E_n^v (E_n^l) is the electric field normal to the interface on the vacuum (liquid) side.[79] Both electric fields are determined by differentiating $\phi(z)$ with respect to z and are averaged among independent simulations. Figure 6(c) shows variations of $|\sigma|$ as a function of $|E_n|$ in positive (orange dots) and negative (blue dots) modes. We can see that the absolute magnitudes of surface charge densities increase as $|E_n|$ increases in general. Based on j_e and σ, the relationship between $\ln(j_e/\sigma)$ and $\sqrt{|E_n|}$ is determined, and the results are presented in Fig. 6(d). The MD data in Fig. 6(d) can be

fitted by using Eq. (10). To do so, we transform Eq. (10) into the following form by taking natural logarithms on both sides

$$\ln\left(\frac{j_e}{\sigma}\right) = \frac{1}{k_B T}\sqrt{\frac{q^3}{4\pi\epsilon_0}\frac{\epsilon_r - 1}{\epsilon_r + 1}}\sqrt{E_n} + \ln\left(\frac{k_B T}{h}\right) - \frac{\Delta G}{k_B T}. \quad (11)$$

From the slope of the fitting curve, one can determine the value of ϵ_r. In Fig. 6(d), we fit the MD data in two regimes under each operating mode. In the low j_e regime, ϵ_r of the RTIL–vacuum interface are found to be 6.28 (positive mode) and 2.56 (negative mode), respectively; in the high j_e regime, ϵ_r of the RTIL–vacuum interface are found to be 1.06 (positive mode) and 1.04 (negative mode), respectively. The decrement of ϵ_r in the high j_e regime compared to that in the low j_e regime origins from the structural changes of the RTIL–vacuum interface at the molecular level under different E_{ext}, as explained in Ref. 58 and in the discussion of Fig. 3 in this work.

The veracity and plausibility of above results are considered from the following aspects. First, to the best of our knowledge, the only available results from MD simulations for the same system in the current literature are from Ref. 58, in which Gromacs package with

Berendsen thermostat and a different approach for maintaining constant electrical potential on electrodes[80] was used. In this work, the results were from a different MD simulation package (ESPResSo) with different thermostats and methods for generating E_n. The agreement between the results from different methods as shown in Figs. 3 and 6 leads to more confidence in the results. Second, apart from simulations, the ion evaporation theory by Iribarne and Thomson was also used in this work to calculate j_e as a function of E_n. The agreement between the results from simulations and theory provides verification of our results from a different perspective. Third, it would be desirable to compare simulations to experiments. However, to our knowledge, experiments with exactly the same system setup (planar electrodes with a planar [BMIM][PF$_6$] film) are yet to be performed, which prevents a direct comparison. Nonetheless, available experimental results in the literature on ion evaporation from Taylor cones of ionic liquids show that the increasing rate of j_e with electric field becomes smaller at higher electric fields,[26,38,81] which agree with our results.

In previous results, E_n is determined by averaging the electric field normal to the liquid surface over all simulation frames. Error bars associated with E_n indicate that, during the course of consecutive ion evaporation events, E_n is not constant, but it fluctuates around a certain value as a function of time. As MD simulation has sufficiently high spatial and temporal resolution to investigate detailed ion evaporation process, we further analyze temporal evolution of electric fields along the trajectory of a typical ion evaporation simulation. Here, the electrical potential difference between the top and bottom electrodes is 80 V, which favors anion evaporation. Figure 7 shows absolute magnitudes of electric fields in the z-direction ($|E|$) at $z = 0.99$ and 36.97 nm as a function of time. The observation duration is 177.2 ps, which contains 21 ion evaporation events. In our study, $z = 0$ nm is defined as the dividing surface position at the RTIL–vacuum interface, where the total number density of cation and anion is half of its bulk value. Both z-positions considered here are in vacuum: $z = 0.99$ nm is near the RTIL–vacuum interface and is the place where E_n is calculated, while $z = 36.97$ nm is near the top electrode. As shown in Fig. 7, E at both z-positions are the same initially. When $t = 10$ ps, $|E|$ at $z = 0.99$ nm decreases abruptly; $|E|$ at both locations then all increases, until $|E|$ at

$z = 0.99$ nm decreases abruptly again when $t = 16$ ps. Subsequently, when $t = 18$ ps, $|E|$ at $z = 36.97$ also decreases abruptly. At later times, temporal evolutions of $|E|$ at both z-positions exhibit similar patterns quasi-periodically. We also compute the difference between electric fields at the two locations (ΔE) by subtracting E at $z = 0.99$ nm from that at $z = 36.97$ nm, and find square-wave-like pulses as shown by the green line in Fig. 7. The increment of ΔE corresponds to the decrement in $|E|$ at $z = 0.99$ nm, while the decrement of ΔE corresponds to the decrement in $|E|$ at $z = 36.97$ nm.

The above observations on temporal evolutions of electric fields can be understood as follows. When an anion is evaporated, the negatively charged anion is separated from the RTIL film, and the RTIL film as a whole becomes positively charged. Considering PBC along x- and y-directions, the evaporated anion, the RTIL film, and their periodic images form two infinite flat sheets with constant surface charge densities. The surface charge density of the sheet formed by the anion (film) is q ($-q$) divided by the cross section area ($A = 7 \times 7$ nm^2) of the simulation system. According to Gauss' law of electrostatics, an infinite flat sheet with a uniform surface charge density of q/A induces an electric field with a strength of $\frac{|q|}{2\epsilon_0 A} = 0.144$ V/nm.[82] The strength of the induced electric field between the two oppositely charged flat sheets is then $|E^*| = \frac{|q|}{\epsilon_0 A} = 0.288$ V/nm, which is exactly the magnitude of pulses in the green line of Fig. 7. When the evaporated ion's z-position becomes larger than $z = 0.99$ nm, the contribution from E^* will be added to the total electric field at $z = 0.99$ nm, resulting in the observed abrupt change in $|E|$. Based on the above discussion, the increment in ΔE represents that an ion has been evaporated from the liquid surface and crosses the plane at $z = 0.99$ nm; the decrement in ΔE indicates that the ion has been within 5 nm away from the top electrode and is removed from the simulation system, as the plane at $z = 36.97$ nm is above the detecting plane for ion removal. By counting the numbers of increments and decrements in the green line of Fig. 7, one can determine the total number of ions that have been evaporated and the number of ions that are present in vacuum at a specific time. Furthermore, by calculating the time interval between adjacent ion evaporation events based on the green line in Fig. 7, we find that the time interval is not constant, but varies as a function of time.
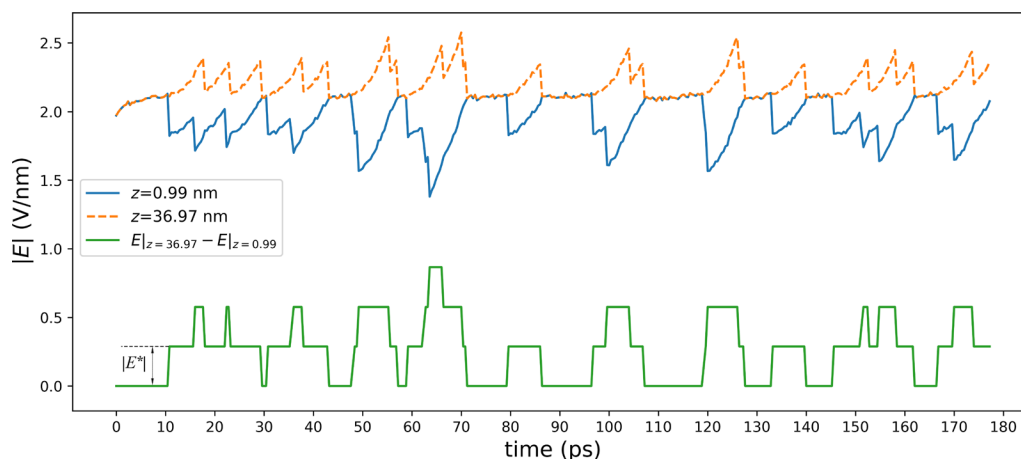

FIG. 7. Temporal evolution of absolute magnitudes of electric fields along the z-direction ($|E|$) at $z = 0.99$ nm (blue) and $z = 36.97$ nm (orange) in a typical constant potential simulation. The difference between E at the two positions is also plotted (green). The potential difference between two electrodes is 80 V and anions are evaporated.

As shown in Fig. 7, after the ion evaporates into vacuum, the strength of electric fields at different z-positions increases, except for abrupt jumps when the ion moves across the detecting plane at $z = 0.99$ nm or it is removed from the simulation system. These increments are caused by the fact that, as the evaporated ion moves further away from the liquid surface, the absolute magnitude of the electrical potential difference due to E^* between the evaporated ion and the RTIL film becomes larger. The potential difference from the evaporated ion to the RTIL film due to E^* and the potential difference from the top electrode to the bottom electrode are opposite in sign. To maintain a constant potential difference between two electrodes, the background electric field needs to increase to counterbalance the potential difference caused by E^*. Such enhancement in electric fields is not observed in constant field or constant charge simulations, which will be discussed later, as these simulations do not enforce constant potential difference between electrodes.

It is also observed in Fig. 7 that at $t = 10$ ps, $|E|$ at $z = 0.99$ nm is highly influenced by E^*, while the increasing rate in $|E|$ at

$z = 36.97$ nm is relatively small. This is caused by several reasons. First, the absolute magnitude of the induced electric field $|E^*| = 0.288$ V/nm is about 15% of the average value (~ 2.0 V/nm) of $|E|$ at $z = 0.99$ nm, so E^* can lead to notable changes in E. Second, right after $t = 10$ ps, $z = 0.99$ nm is between the two infinite charged sheets formed by the evaporated ion and the RTIL film, while $z = 36.97$ nm is not, and hence, E at $z = 36.97$ nm is not affected by E^* at this time. Third, around $t = 10$ ps, the distance along the z-direction between the evaporated ion and liquid surface increases slightly, and the background electric field only needs to increase by a small amount to maintain constant potentials on electrodes, leading to relatively small increasing rate of $|E|$ at $z = 36.97$ nm. We note that this phenomenon occurs in the condition that there are no other evaporated ions in vacuum before the ion evaporates, for example, at $t = 80$ and $t = 133$ ps.

After $t = 16$ ps, the increasing rate of $|E|$ at $z = 36.97$ nm becomes significantly faster compared to the previous interval. This is because the first evaporated ion in vacuum is accelerated by the external electric field, and it moves at a higher speed toward $z = 36.97$ nm
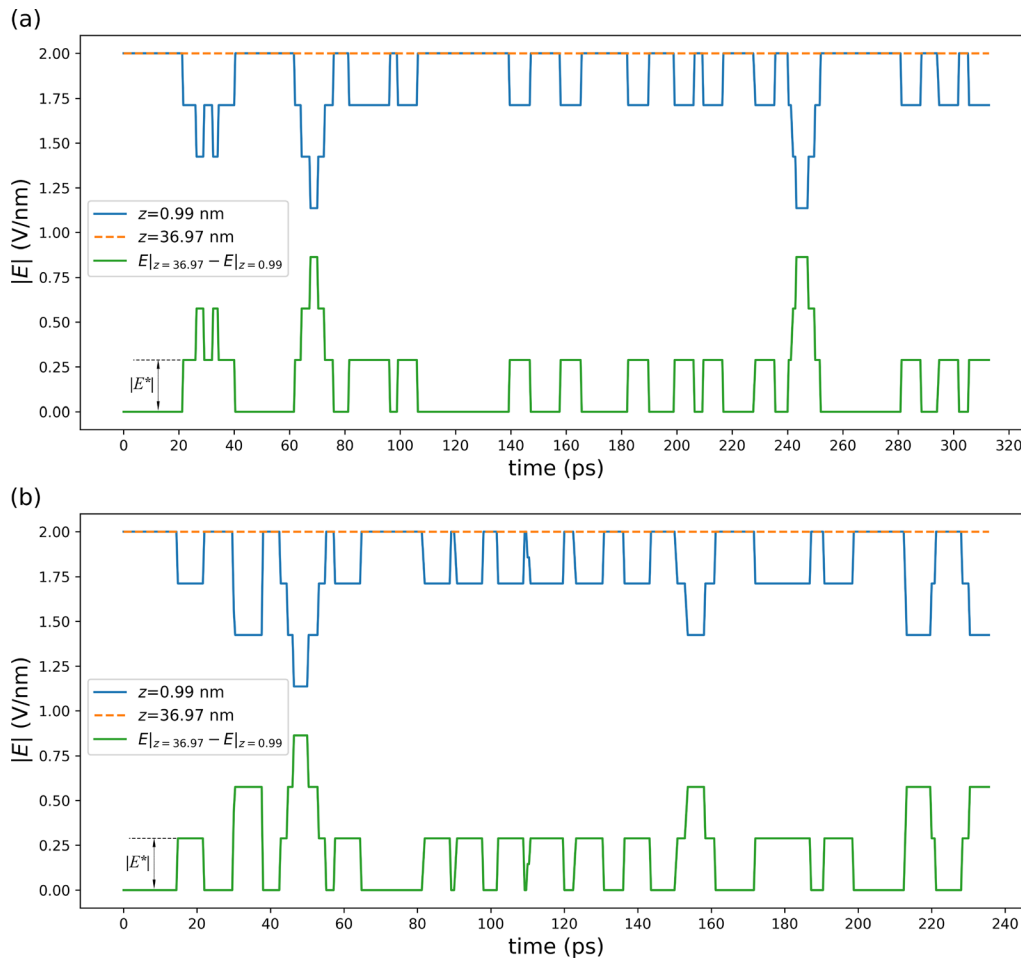

FIG. 8. Temporal evolution of absolute magnitudes of electric fields (E) at $z = 0.99$ nm (blue) and $z = 36.97$ nm (orange) in (a) constant field simulation with $E_{ext} = -2.0$ V/nm, and (b) constant charge simulation with $|s| = 0.018$ C/m^2. The difference between E at the two positions is also plotted (green).

compared to previous intervals. The background electric field then needs to change at a higher rate to maintain constant potentials on electrodes, leading to higher increasing rate of $|E|$ at $z = 36.97$ nm.

In the time interval between $t = 16$ and 22 ps, there are changes in $|E|$, but its increasing rate at $z = 0.99$ nm remains relatively stable. This is caused by the fact that, immediately after $t = 16$ ps, there are two evaporated ions in vacuum. From $t = 16$ to 18 ps, the increasing rate in $|E|$ is dominated by movement of the first evaporated ion, which moves at a higher speed. After $t = 18$ ps, the first evaporated ion moves across the detecting plane near the top electrode and is then removed from the system, causing the abrupt change in E at $z = 36.97$ nm. At this time, the second evaporated ion becomes closer to $z = 36.97$ nm and also moves at a higher speed, leading to similar rate of change in $|E|$ from $t = 18$ to 22 ps.

Figure 8 shows temporal evolution of absolute magnitudes of electric fields at $z = 0.99$ and 36.97 nm in a typical constant field simulation with $E_{ext} = -2.0$ V/nm and in a typical constant charge simulation with $|s| = 0.018$ C/m^2. The difference between electric fields at the two positions (ΔE) is also plotted as green lines in Fig. 8. For the constant field (charge) simulation, the observation duration is 312.8 (235.6) ps with 20 (21) ion evaporation events. We can see square-wave-like pulses in $|E|$ at $z = 0.99$ nm and ΔE, which correspond to events of ion evaporation and ion removal from the simulation system. Different from those in constant potential simulations, the electric fields remain constant between adjacent pulses; $|E|$ at $z = 36.97$ nm is constant over time. The observed differences in temporal evolution of electric fields between constant potential and constant field/charge simulations could lead to differences in the average value and error bar associated with E_n. Nonetheless, the influence of these differences is relatively small, as shown by the good agreement between results under different methods in Fig. 6.

IV. CONCLUSION

In this work, we have studied electric-field-induced ion evaporation from the RTIL–vacuum interface via MD simulations. Ionic current density normal to the interface j_e was calculated as the macroscopic transport property, and its variation under difference E_n was analyzed. The results under Langevin, DPD, and Berendsen thermostats were compared, and it was found that DPD thermostat would be more suitable for simulating ion evaporation, mainly because it avoids applying frictional forces on evaporated ions in vacuum. It was also found that j_e increases as the liquid temperature increases. Several reasons were attributed to this observation, which include higher ionic conductivity, lower viscosity and surface tension, and enhanced thermal fluctuation of the RTIL–vacuum interface.

Effects of different methods for applying E_n on j_e-E_n relationship were compared. In positive and negative operating modes, j_e-E_n curves from constant potential, constant charge, and constant field simulations generally agree with each other. This indicates that, for the type of system considered in this study, easy-to-implement methods (constant charge and constant field) could also be used to investigate the ion evaporation rate.

We also analyzed temporal evolution of electric fields in vacuum. It was observed that the electric fields are not constant over time, and they exhibit quasi-periodic patterns. In each period, the strength of the electric field decreases sharply when the evaporated ion moves across the detecting plane at this position. When the evaporated ion is not crossing the detecting plane, due to its motion toward the top electrode, the strength of electric fields in vacuum all increases in constant potential simulation. These observations were caused by the formation of two charged flat sheets by the evaporated ion and the RTIL film under PBC. Therefore, care needs to be exercised when using PBC for MD simulations of electrospray. The difference between the electric field near the interface and that near the top electrode exhibits square-wave-like patterns, indicating the onset of ion evaporation and the removal of ion in the simulation system.

The results obtained here could guide the selection of proper methods for MD simulations of electrospray in the pure ion regime. This study also lays the foundation to understand more complex ion evaporation phenomena from the RTIL–vacuum interface, or more general the liquid–vacuum interface, at the molecular level.

ACKNOWLEDGMENTS

AUTHOR DECLARATIONS
Conflict of Interest

The authors have no conflicts to disclose.

Author Contributions

Xianzan Tao: Formal analysis (lead); Investigation (equal); Visualization (lead); Writing—original draft (lead). **Xikai Jiang:** Conceptualization (lead); Funding acquisition (lead); Investigation (equal); Writing—review and editing (lead).

DATA AVAILABILITY

The data that support the findings of this study are available from the corresponding author upon reasonable request.

REFERENCES

[1] S. Li, R. Yang, K. Mu, X. Luo, and T. Si, "Thermal effects on the instability of coaxial liquid jets in the core of a gas stream," Phys. Fluids **31**, 032106 (2019).

[2] M. Gamero-Castaño and A. Cisquella-Serra, "Electrosprays of highly conducting liquids: A study of droplet and ion emission based on retarding potential and time-of-flight spectrometry," Phys. Rev. Fluids **6**, 013701 (2021).

[3] B. Guan and R. B. Cole, "The background to electrospray," in *The Encyclopedia of Mass Spectrometry*, edited by M. L. Gross and R. M. Caprioli (Elsevier, Boston, 2016), pp. 132–140.

[4] L. Rayleigh F. R. S, "XX. On the equilibrium of liquid conducting masses charged with electricity," London Edinburgh Dublin Philos. Mag. J. Sci. **14**, 184–186 (1882).

[5] J. Zeleny, "The electrical discharge from liquid points, and a hydrostatic method of measuring the electric intensity at their surfaces," Phys. Rev. **3**, 69–91 (1914).

[6] J. Zeleny, "Instability of electrified liquid surfaces," Phys. Rev. **10**, 1–6 (1917).

[7] G. I. Taylor, "Disintegration of water drops in an electric field," Proc. R. Soc. London, Ser. A **280**, 383–397 (1964).

[8] J. Guerrero, A. J. Hijano, M. A. Lobato, F. J. Higuera, I. G. Loscertales, and A. Fernandez-Nieves, "Emission modes in electro co-flow," Phys. Fluids **31**, 082009 (2019).

[9] F. Cruz-Mazo and H. A. Stone, "Pinch-off of liquid jets at the finite scale of an interface," Phys. Rev. Fluids **7**, L012201 (2022).

[10]A. K. Singh, R. K. Srivastava, and S. S. Bahga, "Regimes of steady jetting in electrohydrodynamic jet printing," Phys. Rev. Fluids 7, 063701 (2022).

[11]H. Huh and R. E. Wirz, "Simulation of electrospray emission processes for low to moderate conductivity liquids," Phys. Fluids 34, 112017 (2022).

[12]J.-B. Cheng, L.-J. Yang, Q.-F. Fu, J.-X. Ren, H.-B. Tang, D.-K. Sun, and X.-F. Sun, "Pulsating modes of a Taylor cone under an unsteady electric field," Phys. Fluids 34, 012007 (2022).

[13]Z. Wang, Q. Kong, B. Li, J. Tian, K. Yu, and J. Wang, "Electrohydrodynamic instability and disintegration of low viscous liquid jet," Phys. Fluids 34, 123301 (2022).

[14]J. Iribarne and B. Thomson, "On the evaporation of small ions from charged droplets," J. Chem. Phys. 64, 2287–2294 (1976).

[15]I. Loscertales and J. Fernández De La Mora, "Experiments on the kinetics of field evaporation of small ions from droplets," J. Chem. Phys. 103, 5041–5060 (1995).

[16]J. Fernández de la Mora, "The fluid dynamics of Taylor cones," Annu. Rev. Fluid Mech. 39, 217–243 (2007).

[17]B. A. Thomson and J. V. Iribarne, "Field induced ion evaporation from liquid surfaces at atmospheric pressure," J. Chem. Phys. 71, 4451–4463 (1979).

[18]D. R. Kingham and V. J. Mifsud, "Focussed ion beams from liquid metal ion sources theory and applications," MRS Online Proc. Libr. 45, 241–246 (1985).

[19]P. Loche, D. J. Bonthuis, and R. R. Netz, "Molecular dynamics simulations of the evaporation of hydrated ions from aqueous solution," Commun. Chem. 5, 55 (2022).

[20]R. Forbest, "Understanding how the liquid–metal ion source works," Vacuum 48, 85–97 (1997).

[21]S. Chapman, "Carrier mobility spectra of spray electrified liquids," Phys. Rev. 52, 184–190 (1937).

[22]S. Chapman, "Carrier mobility spectra of liquids electrified by bubbling," Phys. Rev. 54, 520–527 (1938).

[23]S. Chapman, "Interpretation of carrier mobility spectra of liquids electrified by bubbling and spraying," Phys. Rev. 54, 528–533 (1938).

[24]V. E. Krohn, "Liquid metal droplets for heavy particle propulsion," in Electrostatic Propulsion, edited by D. B. Langmuir, E. Stuhlinger, and J. Seilen (Academic Press, 1961), pp. 73–80.

[25]J. J. McClelland, A. V. Steele, B. Knuffman, K. A. Twedt, A. Schwarzkopf, and T. M. Wilson, "Bright focused ion beam sources based on laser-cooled atoms," Appl. Phys. Rev. 3, 011302 (2016).

[26]I. Romero-Sanz, R. Bocanegra, J. Fernandez de la Mora, and M. Gamero-Castaño, "Source of heavy molecular ions based on Taylor cones of ionic liquids operating in the pure ion evaporation regime," J. Appl. Phys. 94, 3599–3605 (2003).

[27]L. Bischoff, P. Mazarov, L. Bruchhaus, and J. Gierak, "Liquid metal alloy ion sources—An alternative for focussed ion beam technology," Appl. Phys. Rev. 3, 021101 (2016).

[28]R. Burt, K. Breitsprecher, B. Daffos, P.-L. Taberna, P. Simon, G. Birkett, X. S. Zhao, C. Holm, and M. Salanne, "Capacitance of nanoporous carbon-based supercapacitors is a trade-off between the concentration and the separability of the ions," J. Phys. Chem. Lett. 7, 4015–4021 (2016).

[29]T. Kobayashi, A. Kemna, M. Fyta, B. Braunschweig, and J. Smiatek, "Aqueous mixtures of room-temperature ionic liquids: Entropy-driven accumulation of water molecules at interfaces," J. Phys. Chem. C 123, 13795–13803 (2019).

[30]Y. Cheng, J. Zhang, W. Wang, J. Yan, and G. Cai, "Stably electrospraying highly conductive sodium chloride aqueous solution coated with outer ionic liquid using coaxial capillary," Phys. Fluids 34, 093302 (2022).

[31]D. V. M. Máximo and L. F. Velásquez-García, "Additively manufactured electrohydrodynamic ionic liquid pure-ion sources for nanosatellite propulsion," Addit. Manuf. 36, 101719 (2020).

[32]S. Miller, J. Ulibarri-Sanchez, B. Prince, and R. Bemish, "Capillary ionic liquid electrospray: Beam compositional analysis by orthogonal time-of-flight mass spectrometry," J. Fluid Mech. 928, A12 (2021).

[33]X. Suo, K. Zhang, X. Huang, D. Wang, H. Jia, F. Yang, W. Zhang, J. Li, L. Tu, and P. Song, "Electrospray beam currents in the cone-jet mode based on numerical simulation," Phys. Fluids 35, 013603 (2023).

[34]P. Lozano and M. Martínez-Sánchez, "Ionic liquid ion sources: Suppression of electrochemical reactions using voltage alternation," J. Colloid Interface Sci. 280, 149–154 (2004).

[35]B. K. Ku and J. Fernandez de la Mora, "Cluster ion formation in electrosprays of acetonitrile seeded with ionic liquids," J. Phys. Chem. B 108, 14915–14923 (2004).

[36]Y.-H. Chiu, B. L. Austin, R. A. Dressler, D. Levandier, P. T. Murray, P. Lozano, and M. Martinez-Sanchez, "Mass spectrometric analysis of colloid thruster ion emission from selected propellants," J. Propul. Power 21, 416–423 (2005).

[37]Y.-H. Chiu, G. Gaeta, D. Levandier, R. Dressler, and J. Boatz, "Vacuum electrospray ionization study of the ionic liquid, [Emim] [Im]," Int. J. Mass Spectrom. 265, 146–158 (2007).

[38]I. Guerrero, R. Bocanegra, F. J. Higuera, and J. F. de la Mora, "Ion evaporation from Taylor cones of propylene carbonate mixed with ionic liquids," J. Fluid Mech. 591, 437–459 (2007).

[39]C. J. Hogan, Jr. and J. F. de la Mora, "Tandem ion mobility-mass spectrometry (IMS-MS) study of ion evaporation from ionic liquid-acetonitrile nanodrops," Phys. Chem. Chem. Phys. 11, 8079–8090 (2009).

[40]C. S. Perez-Martinez and P. C. Lozano, "Ion field-evaporation from ionic liquids infusing carbon xerogel microtips," Appl. Phys. Lett. 107, 043501 (2015).

[41]F. J. Higuera, "Model of the meniscus of an ionic-liquid ion source," Phys. Rev. E 77, 026308 (2008).

[42]C. Coffman, M. Martínez-Sánchez, F. J. Higuera, and P. C. Lozano, "Structure of the menisci of leaky dielectric liquids during electrically-assisted evaporation of ions," Appl. Phys. Lett. 109, 231602 (2016).

[43]C. S. Coffman, M. Martínez-Sánchez, and P. C. Lozano, "Electrohydrodynamics of an ionic liquid meniscus during evaporation of ions in a regime of high electric field," Phys. Rev. E 99, 063108 (2019).

[44]X. Gallud and P. C. Lozano, "The emission properties, structure and stability of ionic liquid menisci undergoing electrically assisted ion evaporation," J. Fluid Mech. 933, A43 (2022).

[45]K. Misra and M. Gamero-Castaño, "Ion emission from nanodroplets undergoing coulomb explosions: A continuum numerical study," J. Fluid Mech. 958, A32 (2023).

[46]J. W. Daily, "Molecular dynamics simulation of ion emission from nanodroplets of ionic liquids," J. Propul. Power 24, 981–986 (2008).

[47]B. D. Prince, P. Tiruppathi, R. J. Bemish, Y.-H. Chiu, and E. J. Maginn, "Molecular dynamics simulations of 1-ethyl-3-methylimidazolium bis [(trifluoromethyl)sulfonyl]imide clusters and nanodrops," J. Phys. Chem. A 119, 352–368 (2015).

[48]A. Borner, Z. Li, and D. A. Levin, "Modeling of an ionic liquid electrospray using molecular dynamics with constraints," J. Chem. Phys. 136, 124507 (2012).

[49]A. Borner, Z. Li, and D. A. Levin, "Prediction of fundamental properties of ionic liquid electrospray thrusters using molecular dynamics," J. Phys. Chem. B 117, 6768–6781 (2013).

[50]A. Borner, P. Wang, and D. A. Levin, "Influence of electrical boundary conditions on molecular dynamics simulations of ionic liquid electrosprays," Phys. Rev. E 90, 063303 (2014).

[51]N. A. Mehta and D. A. Levin, "Comparison of two protic ionic liquid behaviors in the presence of an electric field using molecular dynamics," J. Chem. Phys. 147, 234505 (2017).

[52]N. A. Mehta and D. A. Levin, "Molecular dynamics electrospray simulations of coarse-grained ethylammonium nitrate (EAN) and 1-ethyl-3-methylimidazolium tetrafluoroborate (EMIM-BF4)," Aerospace 5, 1 (2017).

[53]N. A. Mehta and D. A. Levin, "Sensitivity of electrospray molecular dynamics simulations to long-range coulomb interaction models," Phys. Rev. E 97, 033306 (2018).

[54]N. A. Mehta and D. A. Levin, "Electrospray molecular dynamics simulations using an octree-based coulomb interaction method," Phys. Rev. E 99, 033302 (2019).

[55]N. Nuwal, V. A. Azevedo, M. R. Klosterman, S. Budaraju, D. A. Levin, and J. L. Rovey, "Multiscale modeling of fragmentation in an electrospray plume," J. Appl. Phys 130, 184903 (2021).

[56]J. Asher, Z. Huang, C. Cui, and J. Wang, "Multi-scale modeling of ionic electrospray emission," J. Appl. Phys 131, 014902 (2022).

[57]E. M. Petro, X. Gallud, S. K. Hampl, M. Schroeder, C. Geiger, and P. C. Lozano, "Multiscale modeling of electrospray ion emission," J. Appl. Phys 131, 193301 (2022).

08 April 2024 03:51:02

[58]F. Zhang, X. Jiang, G. Chen, Y. He, G. Hu, and R. Qiao, "Electric-field-driven ion emission from the free surface of room temperature ionic liquids," J. Phys. Chem. Lett. **12**, 711–716 (2021).

[59]X. Yong and L. T. Zhang, "Thermostats and thermostat strategies for molecular dynamics simulations of nanofluidics," J. Chem. Phys. **138**, 084503 (2013).

[60]F. Weik, R. Weeber, K. Szuttor, K. Breitsprecher, J. de Graaf, M. Kuron, J. Landsgesell, H. Menke, D. Sean, and C. Holm, "Espresso 4.0—An extensible software package for simulating soft matter systems," Eur. Phys. J. Spec. Top. **227**, 1789–1816 (2019).

[61]A. Arnold, J. D. Joannis, and C. Holm, "Electrostatics in periodic slab geometries. I," J. Chem. Phys. **117**, 2496–2502 (2002).

[62]J. D. Joannis, A. Arnold, and C. Holm, "Electrostatics in periodic slab geometries. II," J. Chem. Phys. **117**, 2503–2512 (2002).

[63]S. Tyagi, A. Arnold, and C. Holm, "Electrostatic layer correction with image charges: A linear scaling method to treat slab $2D+h$ systems with dielectric interfaces," J. Chem. Phys. **129**, 204102 (2008).

[64]I.-C. Yeh and M. L. Berkowitz, "Ewald summation for systems with slab geometry," J. Chem. Phys. **111**, 3155–3162 (1999).

[65]D. Roy and M. Maroncelli, "An improved four-site ionic liquid model," J. Phys. Chem. B **114**, 12629–12631 (2010).

[66]G. Jeanmairet, B. Rotenberg, and M. Salanne, "Microscopic simulations of electrochemical double-layer capacitors," Chem. Rev. **122**, 10860–10898 (2022).

[67]K. Breitsprecher, K. Szuttor, and C. Holm, "Electrode models for ionic liquid-based capacitors," J. Phys. Chem. C **119**, 22445–22451 (2015).

[68]J. N. Sachs, P. S. Crozier, and T. B. Woolf, "Atomistic simulations of biologically realistic transmembrane potential gradients," J. Chem. Phys. **121**, 10847–10851 (2004).

[69]M. P. Allen and D. J. Tildesley, *Computer Simulation of Liquids* (Oxford University Press, NY, 2017).

[70]P. J. Hoogerbrugge and J. M. V. A. Koelman, "Simulating microscopic hydrodynamic phenomena with dissipative particle dynamics," Europhys. Lett. **19**, 155 (1992).

[71]T. Soddemann, B. Dünweg, and K. Kremer, "Dissipative particle dynamics: A useful thermostat for equilibrium and nonequilibrium molecular dynamics simulations," Phys. Rev. E **68**, 046702 (2003).

[72]P. P. Passler and T. S. Hofer, "Conserving the linear momentum in stochastic dynamics: Dissipative particle dynamics as a general strategy to achieve local thermostatization in molecular dynamics simulations," J. Comput. Chem. **38**, 265–275 (2017).

[73]R. Shi and Y. Wang, "Surface structure of ionic liquids under an external electric field," Mol. Simul. **43**, 1295–1299 (2017).

[74]D. G. Aarts, M. Schmidt, and H. N. Lekkerkerker, "Direct visual observation of thermal capillary waves," Science **304**, 847–850 (2004).

[75]A. P. Thompson, H. M. Aktulga, R. Berger, D. S. Bolintineanu, W. M. Brown, P. S. Crozier, P. J. i 't Veld, A. Kohlmeyer, S. G. Moore, T. D. Nguyen, R. Shan, M. J. Stevens, J. Tranchida, C. Trott, and S. J. Plimpton, "LAMMPS—A flexible simulation tool for particle-based materials modeling at the atomic, meso, and continuum scales," Comput. Phys. Commun. **271**, 108171 (2022).

[76]M. J. Abraham, T. Murtola, R. Schulz, S. Páll, J. C. Smith, B. Hess, and E. Lindahl, "GROMACS: High performance molecular simulations through multi-level parallelism from laptops to supercomputers," SoftwareX **1**, 19–25 (2015).

[77]S. Bi, H. Banda, M. Chen, L. Niu, M. Chen, T. Wu, J. Wang, R. Wang, J. Feng, T. Chen *et al.*, "Molecular understanding of charge storage and charging dynamics in supercapacitors with MOF electrodes and ionic liquid electrolytes," Nat. Mater. **19**, 552–558 (2020).

[78]A. Coretti, C. Bacon, R. Berthin, A. Serva, L. Scalfi, I. Chubak, K. Goloviznina, A. Haefele, B. Marin-Laflèche, B. Rotenberg, S. Bonella, and M. Salanne, "MetalWalls: Simulating electrochemical interfaces between polarizable electrolytes and metallic electrodes," J. Chem. Phys. **157**, 184801 (2022).

[79]J. F. De La Mora and I. G. Loscertales, "The current emitted by highly conducting Taylor cones," J. Fluid Mech. **260**, 155–184 (1994).

[80]A. V. Raghunathan and N. R. Aluru, "Self-consistent molecular dynamics formulation for electric-field-mediated electrolyte transport through nanochannels," Phys. Rev. E **76**, 011202 (2007).

[81]R. S. Legge and P. C. Lozano, "Electrospray propulsion based on emitters microfabricated in porous metals," J. Propul. Power **27**, 485–495 (2011).

[82]E. M. Purcell and D. J. Morin, *Electricity and Magnetism*, 3rd ed. (Cambridge University Press, 2013).

08 April 2024 03:51:02